Numerical investigation of atomisation using a hybrid Eulerian-Lagrangian solver

Pál, Botond; Roekaerts, Dirk; Zandbergen, Barry

DOI
10.1504/PCFD.2021.119266

Publication date
2021

Document Version
Accepted author manuscript

Published in
Progress in Computational Fluid Dynamics

Citation (APA)
Pál, B., Roekaerts, D., & Zandbergen, B. (2021). Numerical investigation of atomisation using a hybrid Eulerian-Lagrangian solver. *Progress in Computational Fluid Dynamics*, *21*(6), 327-342. https://doi.org/10.1504/PCFD.2021.119266

Numerical Investigation of Atomization Using a Hybrid Eulerian-Lagrangian Solver

Abstract: This study investigates the potential of a newly released multi-phase solver to simulate atomization in an air-blast type atomizer. The "VOF-to-DPM" solver was used to simulate primary and secondary atomization in an atomizer with a coaxial injector-like geometry. The solver uses a hybrid Eulerian/Eulerian-Lagrangian formulation with geometric transition criteria between the two models. The conducted study assumed isothermal, non-reacting flow at room temperature. The primary focus was predicting Sauter Mean Diameter and droplet velocity data at a sampling plane downstream of the injection site. The results showed that the solver is able to produce the expected data and to predict trends similar to those found in experimental measurements. The accuracy of the produced droplet diameters was roughly a factor 2 off compared to experiment. This is attributed primarily to mesh resolution. It was concluded that the solver has the potential to predict atomization at a reasonable computational cost, but further study is needed to confirm its full capabilities.

Keywords: Atomization; Ansys Fluent; Multi-phase flow; Spray Formation; Volume of Fluid.

1 Introduction

Predicting atomization in gas-liquid flows is a key challenge relevant to any sector where liquid combustion plays a role. A detailed understanding of the atomization process is a necessity for efficient design of propulsion systems as well as industrial burners. Predicting atomization accurately can be crucial for the design of liquid rocket injectors. Attaining a target droplet diameter at the desired location inside the combustion chamber can increase combustion efficiency and possibly facilitate design of film cooled chambers. In addition, designing throttleable rocket engines also requires knowledge of spray structures at different operating conditions. The work presented in this document is a part of research efforts at TU Delft on the topic of throttleable rocket engines. For most applications, it is desirable to increase the surface area of a droplet relative to its volume. This facilitates mixing and evaporation. From a design perspective, the variables of interest are typically droplet size distribution parameters and droplet velocities (Lefebvre and McDonell, 2017). The typical numerical modeling approach in the past has been to inject a known distribution of droplets into the simulated domain, as explained by Zuzio et al. (2018). This method effectively neglects the dense region of the spray, also known as the primary atomization region. It is commonly defined as the area close to the injection site, where initial breakup occurs. The area where ligaments break up into smaller droplets is referred to as the secondary atomization region. The advantage of such a method is the reduced cost of implementation as compared to a more detailed simulation using interface capturing or interface reconstruction methods (Anez et al., 2019). The result of such a simplification is a diminished predictive capability of the numerical model, since it requires experimental data as an input. Additionally, Shinjo (2018) points out that the primary and secondary atomization regions cannot be considered separately without compromising the physicality of the results. The reason is that the dynamics of a spray are strongly dependent on the manner in which droplets are formed in the primary atomization region. One can therefore conclude, that there is a need for numerical models that take into account both atomization regimes while maintaining a feasible computational cost. In recent years, attempts have been made at developing multi-phase solvers with such a capability. These are hybrid models that switch between continuum (Eulerian) and dispersed (Lagrangian) multi-phase formulations in an attempt to combine the advantages of both.

An example of a hybrid model is the work of Hermann et al. (2010), where the Refined Level Set Grid method is used to track the gas-liquid interface during primary atomization. Separated ligaments that meet size and shape criteria are marked for transition to the Lagrangian model. This process is aided by the use of adaptive grid refinement near the interface. In the Lagrangian model, liquid ligament trajectories are calculated using a point-particle assumption. Recombination of liquid ligaments and the transition of Lagrangian particles back to the Eulerian phase are also included in the numerical model. The author concludes that the algorithm enables a detailed simulation of primary atomization and scales well with increasing processor numbers. Saeedipour et al. (2016) also use an Eulerian-Lagrangian approach to predict the breakup of a round liquid jet. The Eulerian phase is represented using the Volume of Fluid method. Lagrangian droplets are released at the interface using a theoretical criterion based on energy balance instead of ligament geometry. The condition for droplet release is derived from an energy balance between surface eddy turbulent kinetic energy, pressure forces and surface tension. The

model produced favorable qualitative comparisons with experiment for round liquid jets at different pressures. Quantitative comparisons of SMD values also showed favorable agreement with empirical correlations. The work of Zuzio et al. (2018), similarly to Hermann et al. (2010), also uses geometric criteria to remove ligaments from the Eulerian phase and represent them as Lagrangian droplets. The criteria are the characteristic length and volume of a ligament as compared to a sphere superimposed on its center of mass. Recombination of ligaments and a reverse transition from Lagrangian to the Eulerian description are included in the model. The distinguishing characteristic of the solver is the three step process used during transition from the Eulerian to the Lagrangian formulations. During the first step a liquid ligament is identified for conversion. The second step converts the ligament to a particle that still has a volume displacement on the gaseous phase, until it becomes smaller than the finest mesh cell. It is at this point that the conversion to a Lagrangian particle occurs and the volume of the particle is neglected (step three). Results show good qualitative agreement with liquid sheet atomization snapshots. A summary of multi-phase models similar to the ones mentioned so far can be found in the work of Shinjo (2018).

The software suites found in literature that can simulate both primary and secondary atomization via a hybrid model are not available to the public (to the authors' knowledge). The release of Ansys Fluent ver. 19.0 in early 2018 may have been the first publicly available solver that included such a capability. The "VOF-to-DPM" solver, hereinafter referred to as "the solver", is a combination of the Volume of Fluid method and the Eulerian-Lagrangian method. Similarly to the model of Zuzio et al. (2018), geometric and size criteria are used to identify liquid ligaments fit for transition to the discrete phase. The advantages and shortcomings of the approach implemented in the new solver are discussed in the remainder of this paper. The measurement data used throughout this document was provided by the University of Sydney. It is a subset of the Spray Jets and Flames Database found on the webpage of the Clean Combustion Research Group of the School of Aerospace, Mechanical and Mechatronic Engineering (CCRG, 2019). The same dataset was made available to participants of the 7th Workshop on Measurement and Computation of Turbulent Spray Combustion (TCS7, 2019).

The bulk of this work is organized in four chapters. Chapter two summarizes the theory and numerical models that are implemented in the solver. Chapter three describes the geometry of the problem and the simulation inputs. The fourth chapter presents and analyzes the obtained results via comparison with experimental measurements. The fifth and final chapter summarizes the findings of the study and draws conclusions with respect to the merits and drawbacks of the numerical method described herein.

2 Numerical Method

The equations and theory presented in this chapter were extracted from the solver documentation (Ansys Fluent Theory Guide, 2019). The Finite Volume method is used to solve the continuity and momentum equations given by eq. 1 & 2 respectively.

$$\frac{\partial \rho}{\partial t} = \nabla \cdot (\rho \mathbf{u}) \tag{1}$$

$$\frac{\partial}{\partial t}(\rho \mathbf{u}) + \nabla \cdot (\rho \mathbf{u} \otimes \mathbf{u}) = -\nabla p + \nabla \cdot \boldsymbol{\tau} + \rho \mathbf{g} \tag{2}$$

where p is pressure, ρ is density, $\mathbf{u}$ is the velocity vector, μ is dynamic viscosity, $\boldsymbol{\tau}$ is the viscous stress tensor and $\mathbf{g}$ is gravity. The current study investigated isothermal flow. The energy equation was therefore not solved. Turbulence was modeled using a hybrid RANS-LES method referred to as the Stress-Blended Eddy Simulation (SBES) method by Menter (2018). The working principle of the model is based on the use of a proprietary function that determines whether a certain region of the domain uses a RANS or LES turbulence formulation. The SBES model can be viewed as an improved version of the Detached Eddy Simulation model, which introduced the concept of using a RANS formulation in the boundary layer and LES in the core flow (Shur et al., 1999). This technique has lower near-wall mesh resolution requirements compared to a pure LES turbulence model. Turbulence in the RANS region was modeled via the k-ω SST model (Menter, 1994). The subgrid scale (SGS) model of choice was the Wall-Adapting Local Eddy-Viscosity (WALE) of Nicoud et al. (1999). The RANS model was selected since it is regarded as the most accurate version of the k-ω group of models for a wide range of flows (Ansys Fluent Theory Guide, 2019). Similarly, the WALE model was selected based on the recommendation found in the solver documentation. It is stated that the WALE model is more accurate than the Smagorinsky-Lily models and produces the same results as the WMLES model when using the SBES method.

Multi-phase flow was modeled using the Volume of Fluid method (Hirt and Nichols, 1981) and the Eulerian-Lagrangian method. The Volume of Fluid (VOF) model can resolve the flow of two or more immiscible fluids. A single set of momentum equations is solved together with volume fraction equation(s) that specify the volume(s) of different fluids throughout the domain. The volume fraction equation assumes the form shown in eq. 3 for an arbitrary phase b:

$$\frac{1}{\rho_b}[\frac{\partial}{\partial t}(\alpha_b \rho_b) + \nabla \cdot (\alpha_b \rho_b \mathbf{u}_b) = \sum_{a=1}^{n}(\dot{m}_{ab} - \dot{m}_{ba})] \tag{3}$$

where ρ_b is the density of phase b, α_b is the volume fraction of phase b, $\mathbf{u}_b$ is the velocity of phase b, $\dot{m}_{ba}$ is the mass transfer rate from phase b to phase a and $\dot{m}_{ab}$ is the reverse. Equation 3 accounts for an

unspecified number of fluid phases. In the case of this work only two fluids are simulated, which means only one volume fraction equation is solved for the secondary phase (liquid). The volume fraction of the primary phase is obtained from the constraint:

$$\sum_{b=1}^{n} \alpha_b = 1 \tag{4}$$

It is essentially assumed that the volume not occupied by the secondary phase is filled with the primary phase in each cell. The interface is reconstructed using the Piece-Wise Linear Interface Construction (PLIC) method by Youngs (1987). Material properties in each cell are weighted by volume fraction. For a two fluid system consisting of phases a and b, the equation for density is represented by eq. 5:

$$\rho = \alpha_a \rho_a + (1 - \alpha_a)\rho_b \tag{5}$$

All other material properties (viscosity) and properties appearing in transport equations are computed as shown above. Surface tension is modeled using the Continuum Surface Stress model. The surface stress tensor due to surface tension is defined by eq. 6 below:

$$\mathcal{T} = \sigma(I - \hat{n} \otimes \hat{n})|\mathbf{n}| \tag{6}$$

where $\mathbf{n}$ is the volume fraction gradient, $\hat{n}$ is the volume fraction gradient unit vector and I is the identity matrix. The surface tension force is then defined by eq. 7:

$$F = \nabla \cdot \mathcal{T} \tag{7}$$

This model was selected since it is described as superior to the other available model (Continuum Surface Force). Additional discussion on the inadequacies of the CSF model can be found in the work of Baltussen et al. (2014) One of the stated advantages of the CSS model is that it does not calculate surface tension explicitly, which allows it to perform better in under-resolved regions.

2.1 Discrete Phase

The equations presented so far apply to the mixture or Eulerian phase. Additional equations are solved for the positions and velocities of Lagrangian particles. The force balance on a particle in a Lagrangian reference frame is given in Eq. 8:

$$m_p \frac{d\mathbf{u}_p}{dt} = m_p \frac{\mathbf{u} - \mathbf{u}_p}{\tau_p} + m_p \frac{\mathbf{g}(\rho_p - \rho)}{\rho_p} \tag{8}$$

where m_p is particle mass, $\mathbf{u}$ is surrounding fluid velocity, $\mathbf{u}_p$ is particle velocity, ρ is surrounding fluid density, ρ_p is particle density and τ_p is the particle relaxation time. The particle relaxation time, τ_p is defined as:

$$\tau_p = \frac{\rho_p d_p^2}{18\mu} \frac{24}{C_d Re_r} \tag{9}$$

where μ is the kinematic viscosity, d_p is the particle diameter and Re_r is the relative Reynolds number defined as:

$$Re_r \equiv \frac{\rho d_p |\mathbf{u}_p - \mathbf{u}|}{\mu} \tag{10}$$

The drag coefficient is determined using the relation of Morsi and Alexander (1972). Referred to as the "spherical drag law", it uses Re_r and three empirical parameters (a1-a3) to calculate the drag coefficient.

$$C_d = a_1 + \frac{a_2}{Re_r} + \frac{a_3}{Re_r^2} \tag{11}$$

While primary atomization is modeled using the VOF method, secondary atomization is modeled using semi-empirical breakup models that allow the breakup of droplets in the discrete phase. The two models used in this study are the WAVE model (Reitz, 1987) and the Taylor Analogy Breakup (TAB) model (O'Rourke, 1987). Lastly, turbulent dispersion of the discrete phase is modeled using the Discrete Random Walk model of Gosman (1983).

2.2 Gradient Adaption

The solver offers several methods for dynamic mesh adaption. The curvature-based method was used for the purpose of this study, based on a recommendation by the solver authors. The curvature-based gradient adaption method is based on the work of Dannenhoffer and Baron (1985), originally developed to resolve shockwaves. The method is implemented in the solver as given in eqn. 12:

$$|e| = (A_{cell})^{\frac{r_{vol}}{2}} |\nabla^2 \alpha| \tag{12}$$

where e is the error function (adaption function value), A_{cell} is the cell area and r_{vol} is the volume weighting parameter. For the purpose of this study, the volume fraction (α) is the scalar of interest, hence its presence in eqn. 12. Refinement is carried out until the error function value dips below a user defined threshold. The volume weight parameter can be set by the user. It varies between 0 and 1, but the recommended value is 1. If r_{vol} is 1, then the magnitude of the Laplacian of the volume fraction is weighted by a cell length scale equal to the length of one side of a rectangular cell. Weighting is necessary to avoid high error function values in adapted regions, preventing future refinements of coarse areas that have not yet been refined.

2.3 VOF-to-DPM solver

As previously mentioned, geometric criteria are used to transition droplets from the VOF formulation to the Eulerian-Lagrangian one (referred to as DPM in the user guide). What makes the solver unique is the transition criteria it uses to switch multi-phase descriptions. Liquid ligaments/lumps are identified and tracked in the VOF model. Lumps are classified based on asphericity and size criteria defined by the user. When two asphericity criteria and a diameter criterion are met, the liquid lump is converted into a discrete parcel. The two geometrical criteria for transition are a measure of the asphericity of the liquid lump or how closely it resembles a perfect sphere. The first asphericity criterion is the normalized radius standard deviation. The normalized radius is the distance between a facet centroid and the lump center of gravity, divided by the average radius. The second asphericity criterion is the average radius-surface orthogonality. It is defined as the relative orthogonality between the vector connecting the lump centroid to the facet centroid and the facet normal. These two vectors overlap in the case of a perfect sphere. Relative orthogonality ranges from 0 to 1.

When a ligament is removed from the VOF phase and placed into the discrete phase, the volume occupied by liquid for each cell is replaced with an equivalent volume of gas. The solver documentation states that volume conservation is enforced per cell. It is also stated that mass balance will be affected by the mass of the gas added per cell during the conversion process. Since the discrete particles do not impose a volume displacement on the continuum phase, reason dictates that mass is added to the overall domain with every VOF/DPM conversion.

A single liquid lump is converted into a parcel containing a single droplet or less than one droplet based on a setting labeled : "Split any DPM Parcel that Exceeds the Cell Volume by Factor". This setting will be referred to as the Over-Fill Factor (OVF) from this point forward. This parameter controls the factor by which the volume of a converted DPM parcel may exceed the volume of its parent cell. This may happen in cases where the volume of the original (unrefined) cell is less than that of the VOF ligament converted to the discrete phase. Based on the documentation, this feature is necessary to avoid too many discrete parcels forming from a single ligament. A discrete parcel is a droplet representative of a group of droplets that behave similarly. The use of parcels reduces the number of necessary droplet trajectory calculations. Forming several parcels from one ligament can reduce instabilities in the continuous phase solution. If the factor is set to a high value, then more ligaments are converted to a single parcel containing a single particle. A low value means that if the factor is exceeded, a ligament is split into as many parcels as the number of cells that contain it, such that the mass of all the created parcels add up to the mass of the converted VOF ligament.

The authors of the solver specify that the volume of gas introduced into a cell matches the volume of the liquid phase prior to conversion in order to avoid spurious momentum sources and maintain volume conservation. Some ambiguity remains regarding the gas density in the cells affected by the multi-phase transition. It is not specified whether the density of the introduced gas is the same as that of the gas already present or if the density of the cells is kept constant before and after transition. Conservation of momentum dictates that the density of the introduced gas would have to be higher than that of the gas previously present in the cell, if momentum source terms are to be avoided.

If one assumes that the mentioned spurious momentum sources model the momentum received by the mixture phase from the discrete phase, the role of the OVF parameter is clear in the case of two-way coupled simulations. Forming more discrete parcels will result in smaller momentum sources per cell. In the case of one-way coupled simulations (such as the one presented herein), the OVF parameter should then bear no significance with regards to the stability of momentum computation. This is because the continuum phase does not exchange momentum with the discrete phase. The results of this study have found the opposite to be true. This is further discussed in the sections that follow.

It is interesting to note that the OVF parameter is fundamentally a measure of addressing instabilities in the continuum phase solution caused by a lack of mesh refinement. An expensive, but straightforward way of avoiding the ambiguity associated with the OVF setting should be setting it to a value of 1 (ligament volume cannot exceed volume of parent cell) and using a high mesh refinement setting. Allowing cells to be divided enough times during refinement should eliminate the scenario where a ligament exceeds the volume of its parent cell, simply by capturing the formation of ligaments significantly smaller than the original mesh size. Further discussion on this topic is found in the results section.

3 Simulation Setup

The setup of the experiments simulated herein are described in detail in the work of Lowe (2018). The working principle behind the experimental setup is the use of air-blast atomization to stabilize a spray flame for industrial applications. The geometry of the problem is also similar to an element of a coaxial injector used in liquid rocket engines. A central needle injects acetone into a stream of coflowing gas. An additional coflowing gaseous stream surrounds the central pipe containing the needle, referred to as the pilot stream. The needle from which the liquid fuel is injected (acetone) can be moved axially closer to or away from the exit plane, thus allowing control over the fineness of the fuel that comes

into contact with the pilot stream. A cross-section of the geometry is given in Fig. 1 (Lowe, 2018).

Figure 1 Geometry cross-section

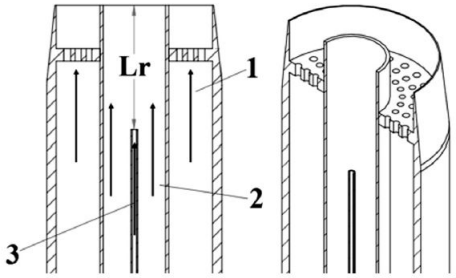

The pilot stream is labeled with the number 1. The needle injecting the liquid and the surrounding coflow are labeled 3 and 2 respectively. Fig. 2 shows the simulation domain with dimensions provided in mm. The needle and coflow inlet were taken roughly 7 coflow diameters upstream from the needle exit plane. This was a compromise between a length sufficient to let the boundary layer fully develop but small enough not to require an excessive number of cells. The 25mm distance from the needle exit plane to the coflow exit plane is referred to as the needle recess length (L_r) and matches the experimental setup. The recess length for the simulation was chosen based on the domain size requirement and the adequacy of the resulting flow field to test the capabilities of the numerical method on modeling primary and secondary atomization concurrently. A configuration with a longer recess length would've required a sizable computational domain (since measurements were taken at the needle exit plane). Such a configuration may have also increased the dependence of the results on the wall-droplet interaction model. If that were the case, it would be difficult to evaluate the ability of the numerical model to produce an accurate droplet distribution. The chosen experimental configuration produces a spray that is close to (but not fully) atomized - measurements indicate that 92.5% of liquid shapes are spherical droplets at the measured location (Lowe, 2018). It is for this reason that the data set can be used to test not only the solvers capability to predict droplet sizes, but also atomization regime.

It is worth noting that the wall thickness of the coflowing stream was neglected for the purpose of the simulation. The thickness of the needle wall was taken into account. The inlet of the pilot flow was placed at the exit plane of the coflow. This was also a compromise in an effort to reduce cell count. Placing the inlet at this location does not allow the wall boundary layer to develop, so the most accurate setup would necessitate a velocity profile specification. Due to the low velocity of the pilot stream with respect to the coflow stream, it is reasonable to assume that the effect of the pilot inlet placement is not as significant as the other inlets. The distance from the pilot inlet to the exit plane was based on cell count and reverse flow balance. If the outlet is too close, reverse flow may be encountered, which can alter the simulation results. A value of 5 pilot stream diameters was found to be a reasonable initial value for this length.

A front view is provided as a reference, to show that the domain is cylindrical. The perforated plate in the pilot stream (see Fig. 1) is not visible since it is not included in the geometry (pilot inlet plane coincides with the coflow exit plane). The most important geometrical parameters are summarized in Table 1.

Table 1 Simulation Geometry

Parameter Name	Value (mm)
Needle diameter (D_n)	.686
Coflow diameter (D_c)	10
Pilot diameter (D_p)	25
Needle wall thickness	.1905
Needle recess length	25

To summarize, in an effort to keep a reasonable cell count, the domain has a number of simplifications and shortcomings. These are the areas that will need refinement in a domain sensitivity study. The thickness of the wall between the coflow stream and the pilot stream was neglected (infinitely thin). The distance to the outlet from the pilot inlet could be increased up to 10-20 pilot diameters. The distance between the coflow inlet and the needle outlet could also be increased up to 30-40 diameters. These estimates are based on common values found throughout literature. The radius of the domain after the exit plane could also be a variable in a domain size sensitivity study. It is worth noting that the entire assembly was placed in a vertical wind tunnel when the measurements were taken. Extending the domain radially will mean modeling an additional coflow at a different speed which may or may not increase the complexity of the simulation significantly.

A summary of the operating conditions and material properties can be found in Table 2. All velocities are normal to their respective inlets. Material properties are provided by the authors of the experiment. Relevant non-dimensional numbers such as the Reynolds and Weber numbers are also provided for reference. The values seen in Table 2 can be found in the document describing the experimental database of the Sydney Needle Burner (TCS7, 2019).

The momentum ratio (M) is a commonly defined metric for atomization studies alongside the Weber and Reynolds numbers. It is important because it is a measure of the relative momentum between the two fluid streams.

$$M = \frac{\rho_g u_g^2}{\rho_l u_l^2} \tag{13}$$

Figure 2 Simulation domain (not to scale)

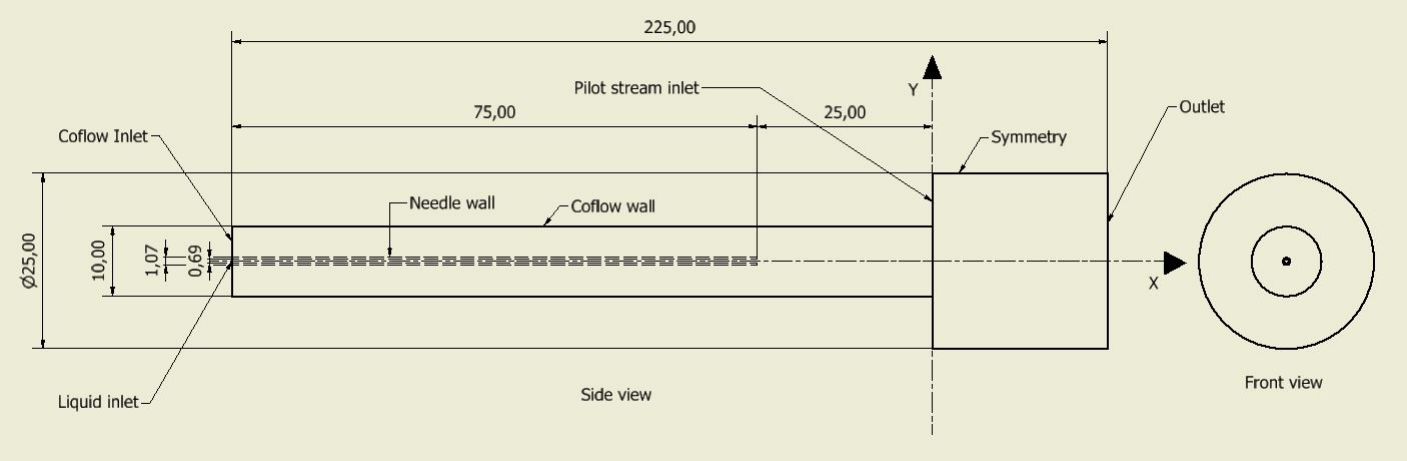

Table 2 Simulation Parameters

Parameter Name	Value
Liquid bulk velocity	2.58 m/s
Air bulk velocity	48 m/s
Liquid density	786 kg/m^3
Air density	1.225 kg/m^3
Liquid viscosity	3.33e-04 Pa s
Coflow Reynolds nr	28374
Liquid Reynolds nr	4180
Chamber temperature	293 K
Absolute Pressure	1 bar
Surface tension	.0237 N/m
Weber number	80
Momentum ratio (M)	.53
Mesh topology	Hexahedral
Mesh count (original)	450000 cells

The Weber number in Table 2 is defined by the experimenters as (Lowe, 2018):

$$We = \frac{\rho_g u_g^2 D_n}{\sigma} \tag{14}$$

3.1 Mesh overview

The general meshing strategy was based on two goals: ensuring high resolution in the areas of primary atomization and keeping a structured mesh to reduce cell count. Fig. 3 shows a side view of the mesh. The gradual decrease in cell size in the axial direction can be seen from the coflow inlet plane towards the needle exit plane. The same is true for the resolution variation from the outlet to the pilot inlet. It is easy to see that the cell aspect ratios are high at the inlets on the far left and the outlet on the far right of Fig. 3. These are areas that can use refinement.

Figure 3 Mesh side view

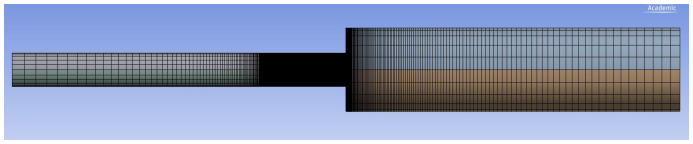

A front view of the mesh seen in Fig. 4 shows that the mesh is finest at its center and the cell sizes gradually increase radially outwards. Again, the rationale was to have the highest resolution in the region where primary atomization occurs. The quickly increasing aspect ratio of the cells in the radial direction is easily visible here. Refinements in the radial direction are the most expensive from a total cell count point of view, since the mesh has the same cross section (cell shape and layout) at every axial point.

Figure 4 Mesh front view

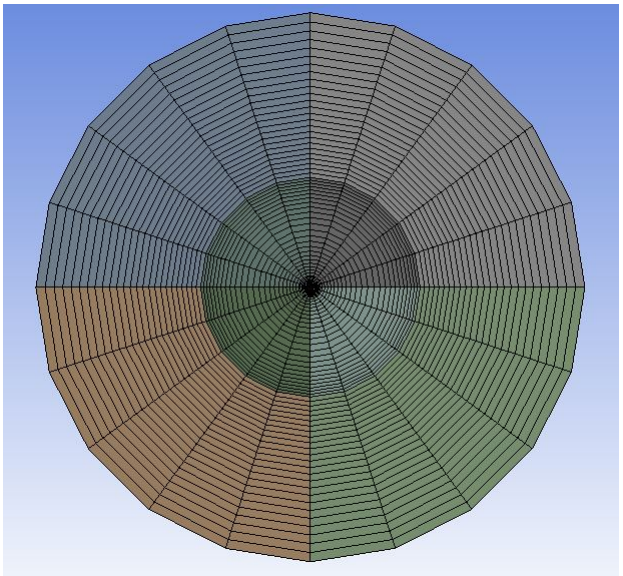

Fig. 5 shows the upper-half of the mid-plane of the domain in the region after the needle exit plane and before the pilot inlet plane. The dense region towards the bottom is the centerline of the domain. The cell aspect ratio is highest in the middle (between the wall and centerline), this was done to manage the cell count while maintaining adequately small cells near the wall to ensure a correct shear stress prediction. (Note: The difference in contrast between some of the vertical lines is an unintended software glitch and bears no significance).

Figure 5 Mesh mid-plane view

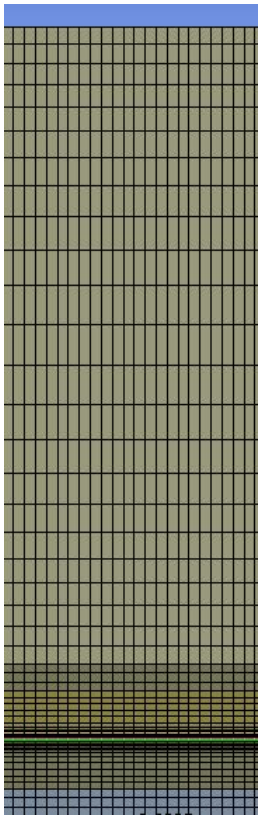

The total initial cell count in the domain was 450000 hexahedral cells. This is a relatively low amount by any measure (as most LES simulations in literature are in the range of 2-3 million cells). It is important to note however, that the cell count can increase significantly depending on the mesh adaption settings. In addition, the simulation makes use of a hybrid RANS-LES turbulence model which makes the resolution requirements lower than those for LES. The final cell count after adaption remained about 510000.

It should be possible to estimate the sizes of the droplets that the mesh will be able to resolve using geometrical reasoning. Because the diameters of the discrete parcels are determined by the ligaments that the VOF model is able to resolve, a relationship can be established between the resolution of the mesh and the smallest resolved parcels. The structure of the mesh is such that the length of the cells in the x direction, from the exit plane of the needle to the exit plane of the burner, is constant. Cell edges in the y direction are not constant. In the circumferential direction, cell sizes are constant. Knowing that cell edge lengths must be smaller than the size of the particle in order to capture its geometry, it can be said that the largest edge length will determine the smallest particle that can be captured. Fig. 6 shows a closeup of the mesh around the needle exit plane:

Figure 6 Needle exit plane side view

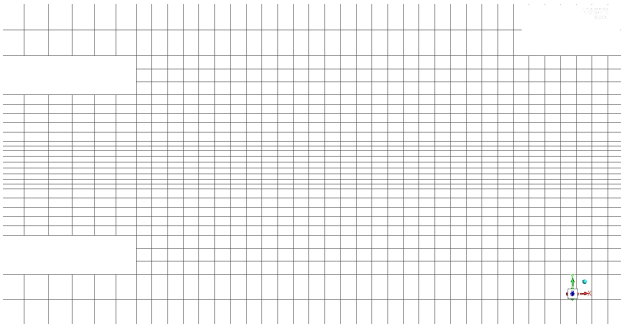

Knowing the diameter of the needle (686 μm), estimates can be derived for the edge lengths of the cells. Fig. 4 also clearly shows that there are 20 divisions in the circumferential direction in total. Using the radius of the needle, an estimate can be obtained for the circumferential edge lengths at the walls of the needle. Using hanging node refinement and a maximum refinement level of 2, it is possible to estimate the smallest refined edge length. If it is further assumed that a minimum of two edges are required in each direction to capture a spherical ligament, an estimate of the smallest resolvable diameter can be obtained. This data is shown in Table 3. One can conclude based on the presented estimates, that in the best case scenario, the smallest droplet diameter that can be resolved in the primary atomization zone is about 86 μm.

Table 3 Mesh resolution

Direction	**X** (μm)	**Y** (μm)	**Circumf.** (μm)
Base mesh	45	90	172
Refined 2x	11.25	22.5	43
Smallest resolvable diameter	22.5	45	86

All simulations were run on a single Dell Precision T5600 machine. Eight to sixteen cores were run in parallel on the Intel Xeon E5-2665 processor. Since the presented study was done as preliminary work with the goal of gauging the capability of the solver, the available computational resources were limited. The numerical setup was designed with this limitation in mind.

4 Results & Validation

This section is organized into three subsections. The first one discusses the variables of interest and the location and manner in which they were recorded. Simulation results at locations of interest are presented. The second subsection discusses the results of sensitivity studies and the results on variables of interest. The third section validates the obtained results using experimental data.

4.1 Droplet Size and Velocity Results

Measurements of parcel properties were carried out by defining a sampling plane at an axial distance from the burner exit plane that matches the location of experimental measurement. The properties of any discrete parcels that pass through the sampling plane are recorded. In this case, sampling was done over a plane parallel to the exit plane at a distance of X/D_c=0.3 in the positive x direction from the burner exit plane. The coordinate system origin is at the center of the burner exit plane (see Fig. 2). Because primary and secondary atomization are modeled in the simulation, there is a relationship between parcel sizes and velocities. Both are also primarily functions of the continuum phase velocity magnitude. For this reason, it is wise to examine the velocity field inside the burner. Figure 7 shows the mean axial velocity of the mixture phase radially across the exit plane.

Figure 7 Mixture axial velocity magnitude at exit plane

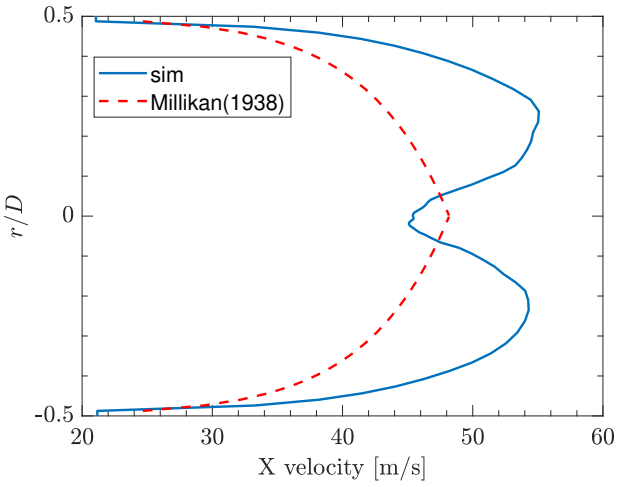

The profile is almost perfectly symmetrical about the centerline. The reason for the slight asymmetry is likely due to liquid ligaments passing through at slower velocities than that of the gas. Near the centerline there is a decrease in velocity. This can be explained by the presence of slower moving liquid ligaments in the core and their wakes. The two peaks are roughly halfway between the centerline and the wall, which intuitively makes sense because on either side there must be slower moving liquid (wall on the outside and low velocity liquid in the core). Examining the near-wall region, the shape of the velocity profile resembles the typical turbulent velocity boundary layer and reaches zero at the wall (per the no-slip boundary condition). A comparison with the relation for the overlap layer velocity for turbulent pipe flows proposed by Millikan is included for reference (Millikan, 1938). The profile is given by Eq. 15:

$$\frac{u(y)}{u^*} = \frac{1}{\mathcal{K}} ln \frac{(R-y)u^*}{\nu} + B \tag{15}$$

where u^* is friction velocity, y is the distance from the centerline, R is the coflow stream radius, ν is kinematic viscosity and $\mathcal{K}$ and B are constants. The empirical profile assumes turbulent pipe flow at a Reynolds nr. equivalent to that of the coflowing stream. Close to the wall, there is reasonable agreement between the two curves. Moving away from the wall, the velocity of the empirical profile consistently predicts a lower value possibly due to the effect of the pilot stream.

Fig. 8 portrays SMD values across the coflow radius. Each data point is plotted at the center of the radial interval over which the discrete parcels were recorded, where $r^2 = y^2 + z^2$. For example, the SMD value of 132 at r/D_c=.56, represents the Sauter Mean Diameter of all the particles recorded over the interval r/D_c=[.5,.6]. SMD values are highest at the center line and decrease in the peak velocity area. Values then increase with the radial coordinate and decrease towards the end of the measurement area. The decrease seen above the r/D_c=.5 height could be the result of an increase in turbulence intensity due to the mixing layer formed by the interaction of the pilot stream with the coflowing stream.

Figure 8 Droplet SMD at X/D_c=.3

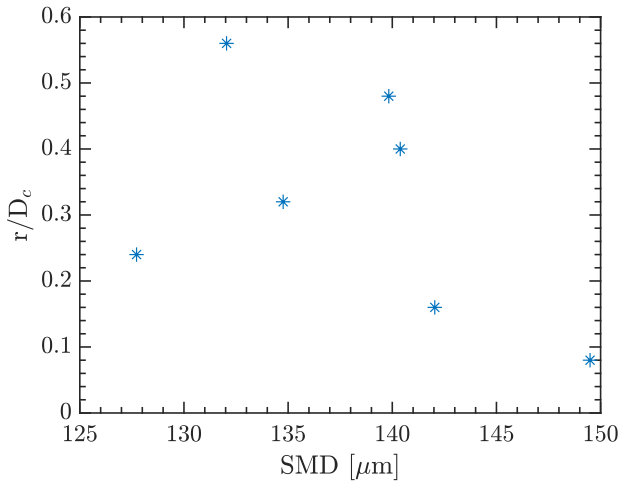

Because the break-up model is based on the relative velocity between liquid and gas, one would expect an inverse pattern of diameter vs height to the pattern seen in Fig. 7. Physically, this also makes sense since higher

Weber numbers (or higher inertial to viscous force ratios) will act to destabilize ligaments and initiate breakup.

Figure 9 Mean droplet axial velocity at X/D$_c$=.3

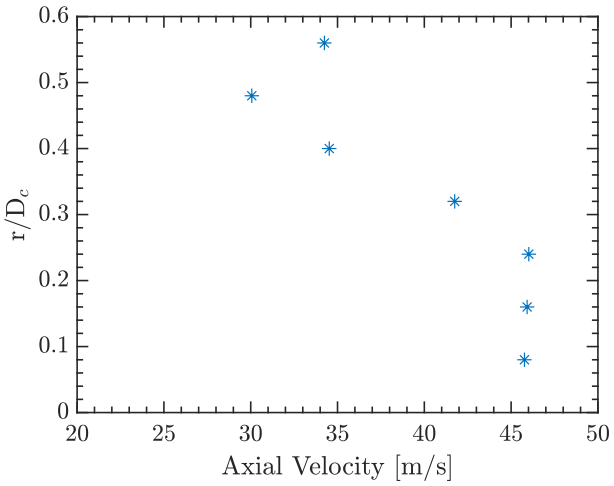

Figure 10 Flow axial velocity at X/D$_c$=.3

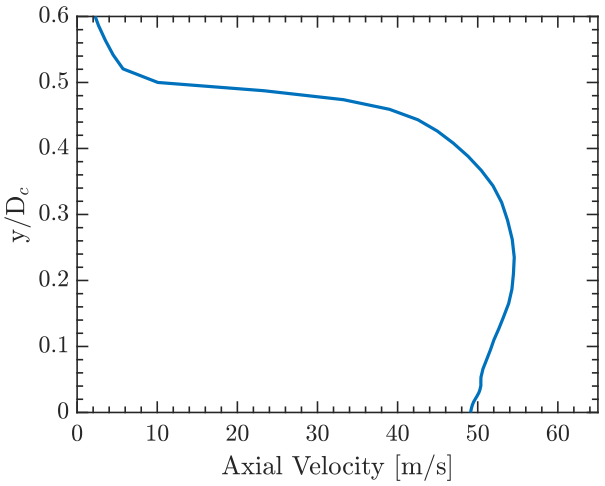

The velocity of the droplets is a function of drag. Considering the physics of the studied problem, the expected trend is that the droplets will accelerate in the axial direction and eventually reach the bulk velocity of the flow. This process is complicated by breakup, because smaller droplets will react differently to a disturbance than larger droplets. If one examines the mean flow velocity vs the mean droplet velocity in the radial direction, the pattern should be similar even if the particles have not yet reached the flow bulk velocity. Fig. 9 shows the mean droplet axial velocity across the radial direction. Intuitively the pattern looks reasonable since velocities decrease radially outward with a slight increase at the last point, which may be a result of the pilot stream momentum.

A comparison with the flow velocity at the same locations, seen in Fig. 10, shows some discrepancies. At the top of the curve, there is a noticeable difference in the magnitude of the flow vs the magnitude of droplet velocity. This is likely caused by the fact that the pilot stream velocity is about 2.5 m/s, which is the velocity seen above r/D=.5. The droplets in this region have presumably retained most of their energy picked up from the coflow of the burner. This would explain the significantly higher droplet velocity (compared to the flow mean velocity) at heights above r/D=.3.

To illustrate the transition mechanism and the interface topology, a visualization of the liquid phase surface inside the atomizer can be seen in Figs. 11-13. Figure 11 shows the 0.5 volume fraction isosurface of the liquid jet at the breakup point (green). The colored particles are dispersed phase droplets colored by diameter. Inside the red circle is a ligament still in the VOF phase with visible mesh refinement around it. Figure 12 illustrates the same view a short time after the mentioned liquid ligament is transitioned into the discrete phase and the mesh is coarsened to its original size.

Figure 11 Ligament before transition

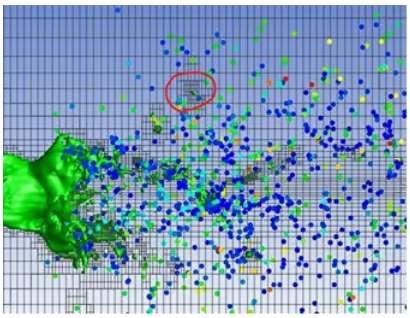

Figure 12 Ligament after transition

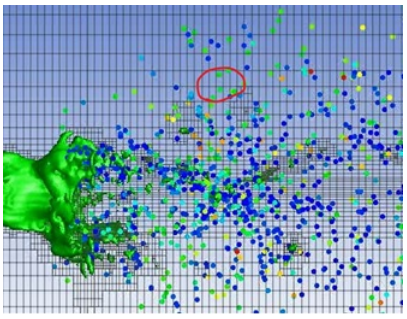

Figure 13 shows the 0.5 volume fraction isosurface with the dispersed phase hidden, for reference. On the left side of the figure, the exit plane of the needle is visible. The mesh seen in the background is at the mid-plane of the domain.

Figure 13 0.5 volume fraction isosurface

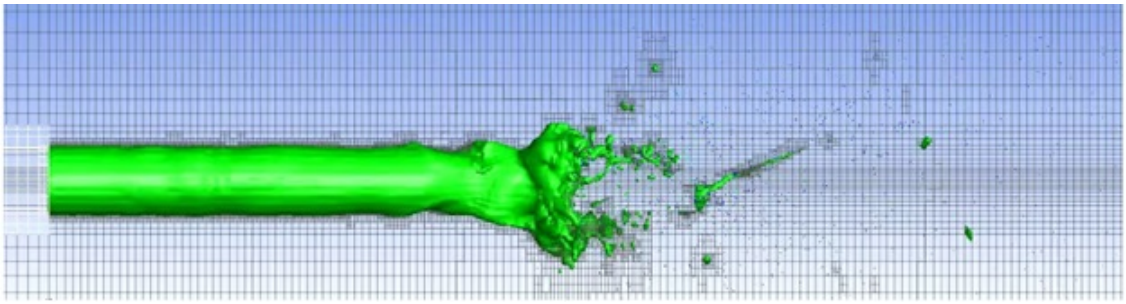

4.2 Sensitivity studies

A comparison of results obtained using different settings or physical models can shed light on the accuracy of the results as well as the adequacy of the implemented models to the problem being solved. Table 4 summarizes the different simulations conducted and the changes made as compared to the control simulation.

Table 4 Simulations Summary

Simulation nr.	Parameter varied	Values
1	Control	N/A
2	Overfill factor	From 2 to 1
3	Breakup model	From WAVE to TAB
4	Cell count	540000 to 2400000

4.2.1 Over-Fill Factor

The Over-Fill Factor was chosen as a parameter for a sensitivity study because it is fundamental to the transition mechanism of the solver. As previously mentioned, the OVF governs the number of parcels that are formed from a liquid ligament. Because mass conservation is enforced, it subsequently also governs the diameters of the parcels that are formed. Fig. 14 shows SMD results at an OVF value of 2 compared with an OVF value of 1. Fig. 15 shows the axial velocities of OVF-1 and OVF-2 data sets seen in Fig. 14.

Based on the description of the OVF parameter, a smaller value should result in ligaments being converted into multiple smaller discrete parcels as opposed to a single one. This is not what the results indicate. SMD values for OVF-1 are only smaller at 2 out of the 7 locations in question. One explanation may be an incorrect velocity prediction in the cells that liquid was removed from. In order for this to be the case, however, velocity predictions should be low. The low velocities could prevent parcel breakup. It is not clear how this may happen however. In case a source term inserts an amount of gas with the same volume as the removed liquid, the cell sees a net decrease in mass. This should then result in an over-prediction of velocity, when momentum conservation is enforced. The high velocity may then accelerate and cause the newly formed parcel to break up prematurely (through the secondary breakup model). This should then still result in smaller parcels forming for smaller OVF values.

Figure 14 SMD distribution at X/D_c=.3

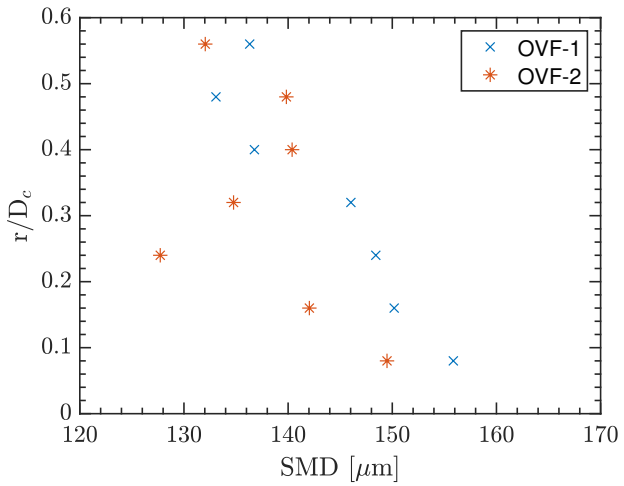

Figure 15 Mean droplet axial velocity at X/D_c=.3

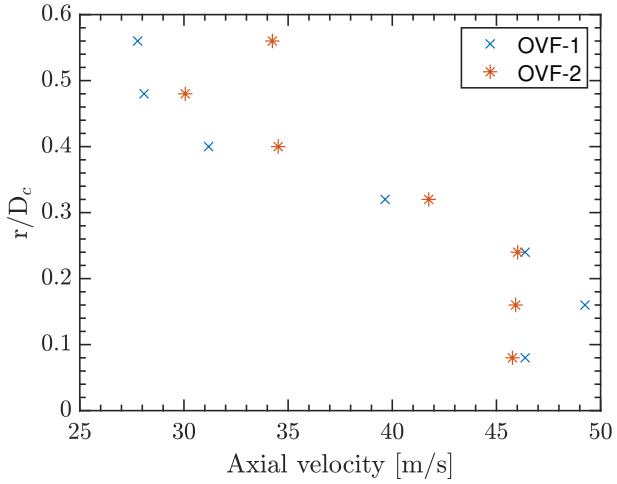

Discrepancies are also noticeable in the droplet velocity distribution. Larger particles should take longer to react to the velocity of the flow and therefore the expectation is that the velocities of OVF-1 be smaller than those of OVF-2 for locations where the SMD is smaller. Again, this does not apply for all locations. This phenomenon also reinforces the notion that an incorrect prediction of parcel velocities may have occurred during the conversion process. Apart from the analysis presented so far, it is worth noting that lower OVF values have resulted in a significantly stabler simulation. The chance of divergence diminished significantly as the OVF parameter was decreased.

4.2.2 Breakup models

The breakup model of the discrete phase is essential in correctly predicting secondary atomization. It was therefore decided to include a sensitivity study focusing on two classical breakup models (WAVE and TAB). The software theory guide claims that the WAVE model is applicable for Weber numbers above 100 and the TAB model is effective for "low Weber number" sprays. Based on this information only, a sensitivity study using these two models could shed light on the limits of the influence of secondary breakup modeling on droplet sizes. The reader is reminded that the Weber number of the studied case is 80. Standard constants were used with both breakup models. Figs. 16 and 17 show SMD and axial velocity results at the plane of interest (X/D_c=.3).

Figure 16 SMD distribution at X/D_c=.3

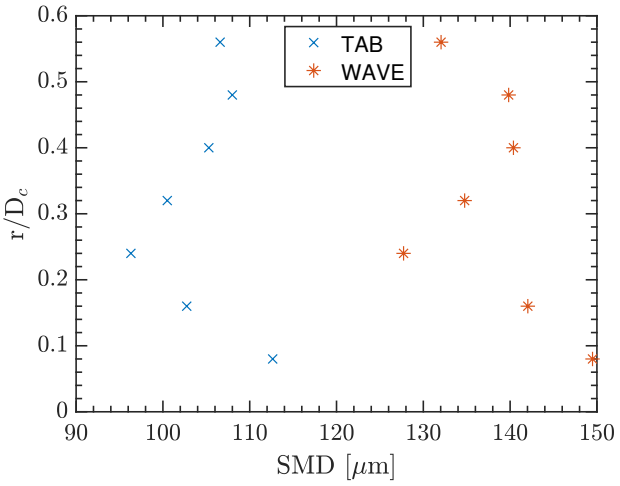

It is clear that the TAB model has produced smaller SMD values at all radial height intervals. Reason then dictates that velocity values would be the same as the WAVE model velocities or higher, due to smaller droplets reacting to the flow in a shorter time. However, this is only true if breakup has occurred far upstream of the location of measurement. The velocity results indicate lower velocity values for the TAB model at almost all heights. Another significant difference is the shape of the

Figure 17 Mean droplet axial velocity at X/D_c=.3

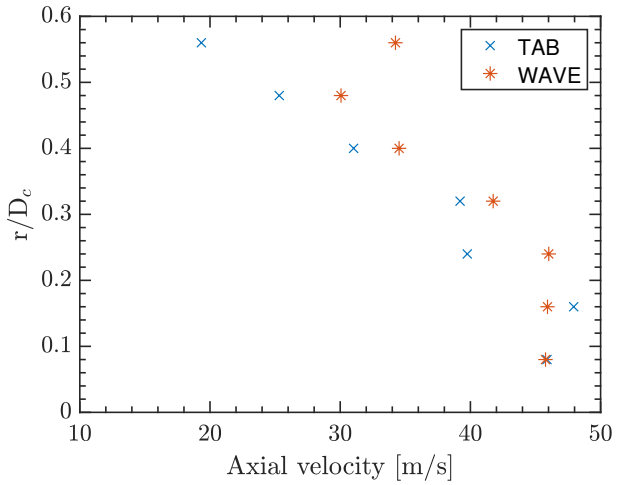

velocity curve, which shows a decrease between the last two data points for the TAB model. This difference will be significant for validation purposes.

Having examined the results, the fundamental question becomes: why does the TAB model predict smaller droplet sizes than the WAVE model? Some possible answers can be found in the original work on the TAB model by O'Rourke and Amsden (1987). It is stated that one of the advantages of the TAB model over the WAVE model of Reitz (1987) is the inclusion of the effect of liquid viscosity. Another mentioned advantage over the WAVE model is the ability of the TAB model to predict that breakup does not necessarily occur at a well defined critical Weber number. Since the Weber number for the problem in question is below the recommended range for the WAVE model (above 100), it is to be expected that the results will not be optimal. The difficulty lies with the intermediate Weber number range of the problem, which is likely not the ideal range for the TAB model either (it is too high). Future studies could be conducted on the appropriateness of other breakup models for the studied experiments.

4.2.3 Mesh sensitivity

The most important concern of the CFD user when it comes to creating the mesh should be discretization error. This is the error that results from representing governing equations as algebraic expressions over a discrete domain of space and time. Temporal discretization error is a function of the time-step size used. Discretization error is a function of the quality of the grid. Quality metrics of relevance are: resolution, density, orthogonality, aspect ratio etc. In cases where the implemented equations do not depend on the grid size directly (RANS models), a mesh convergence study can be carried out in order to determine the resolution at which the solution becomes "grid independent". In these cases, the discretization error tends to zero as the grid size tends to zero. In cases where equations for physical

models depend on the grid size directly (LES turbulence models), a different approach must be taken to error quantification. Due to the hybrid turbulence model used, changing the mesh size will directly affect the results obtained since the filter size changes. It was considered important to determine the extent of drop size and velocity sensitivity to mesh resolution. A simulation was carried out using the settings of Simulation nr.1, but on a finer mesh of roughly 2.5 million cells (after refinement). Using the same reasoning as in Table 3, the smallest resolvable diameter determined by the circumferential mesh size is 46.5 μm. Figs. 18 & 19 show the results compared to the results of Simulation nr.1.

Figure 18 SMD distribution at X/D_c=.3

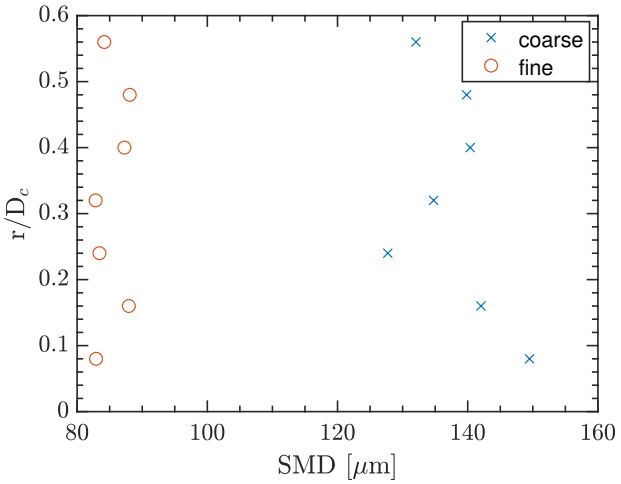

Figure 19 Mean droplet axial velocity at X/D_c=.3

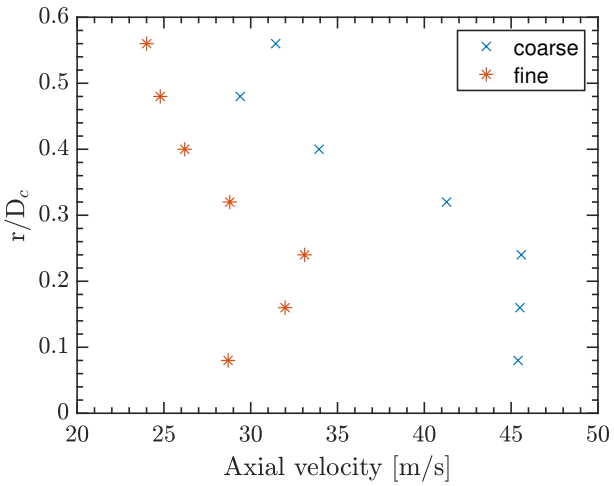

There is a clear decrease of SMD values at all radial locations in the case of the finer mesh. This is explained by a finer mesh allowing smaller ligaments to be resolved. The general shape of the SMD distribution did not change between the two curves. Regions of increasing and decreasing SMD values remained consistent. The range between the smallest and largest SMD values recorded has narrowed in the case of the finer mesh. The axial velocity curve obtained from the fine mesh shows a quantitative and qualitative change in the distribution. Velocity values have decreased at every axial location. This may be counter-intuitive at first, since it is known that smaller particles react quicker to disturbances in the flow-field. Since both the SMD values and velocities have decreased, it is likely that the flow-field has changed significantly due to the change in filter size. The shape of the curve has changed from a nearly vertical region near the centerline to an increasing one. The distribution at the top of the velocity curve has also changed compared to the coarser mesh. These findings will become relevant for validation purposes.

4.3 Validation

This section will compare the properties of the droplets sampled during simulation with experimentally measured values. The reader is reminded that during the simulation, all droplets were sampled at a plane normal to the burner exit plane and at an axial distance such that X/D_c=.3. SMD values were calculated for the group of droplets obtained per radial interval. Velocity values were averaged over all the droplets in a radial interval. Fig. 20 presents the SMD results of Simulation nr. 1 labeled "coarse" vs Simulation nr. 4 labeled 'fine' vs experimental measurements labeled "exp".

Figure 20 SMD validation - Sim 1 & Sim 4

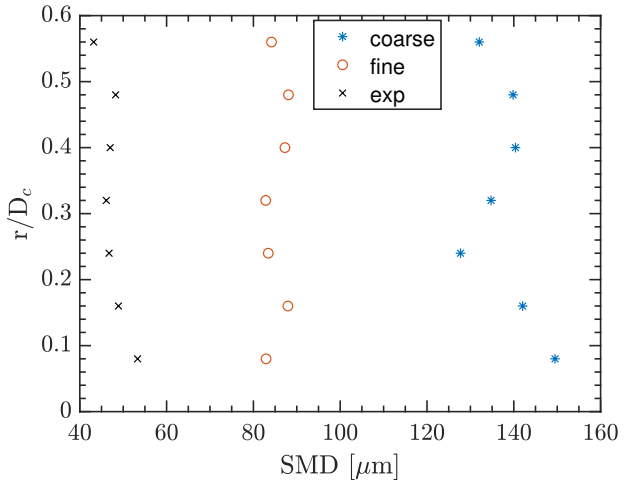

The SMD values of Simulation 1 (coarse) exceeded measured values roughly by a factor three. Qualitatively, the shape of the SMD curve agrees with that of experiment. There is a decrease in SMD from the centerline to about the .25 radial location. This is followed by an increase up to the last two data points, where SMD values once again decrease. The results from Simulation 4 (fine) demonstrate high mesh dependence. The curve is about a factor 2 off with respect to

experiment. In addition, there is a change in the distribution shape near the center line of the burner. This may be a result of several phenomena such as: changes in the calculated flow-field or changes in the behaviour of the transition mechanism. One explanation might be that due to the finer filter applied in the LES region near the center line, ligaments break off from the core earlier. This may result in earlier transition to the discrete phase and secondary breakup. More studies are required to properly identify the causes for this change.

Figure 21 Axial velocity validation - Sim 1 & Sim 4

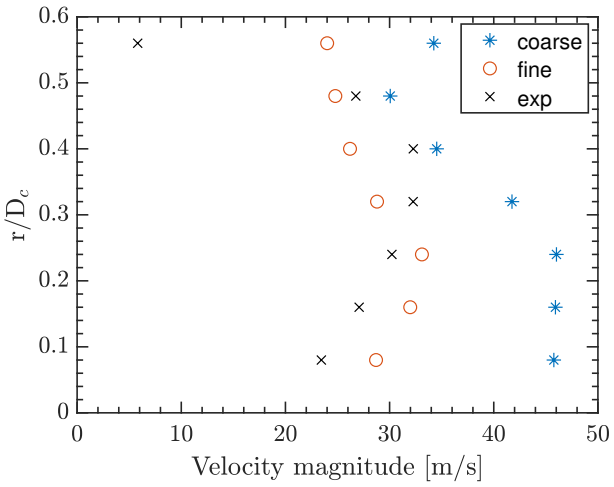

Figure 21 presents average droplet axial velocities vs. experiment. There is a significant qualitative improvement in the shape of the curve when using the finer mesh, as compared to experiment. The vertical profile near the centerline, found in the coarse results, is no longer present. An increase in axial velocity in the radial direction is correctly predicted instead. A decreasing tendency is also correctly predicted past the r/D$_c$=0.3 radial location, but there is still a significant discrepancy from experiment near the highest radial location. Given that mesh resolution decreases radially outwards, it is likely that discretization error plays a significant role in the discrepancy with experiment. The geometrical simplification of neglecting the thickness of the pilot stream outer wall is also likely affecting the quality of the results.

The results of Simulation nr. 3 (breakup model switch from WAVE to TAB) showed significant changes compared to the control case. A decrease of the order of 30 μm can be seen in Fig. 16 when using the TAB model vs. the WAVE model. For reference, the results of Simulation 3 compared to experiment can be seen in Figs. 22 & 23.

The radial SMD profile is a good qualitative match with experiment. The velocity profile shows a decreasing trend with an increase in radial location, while remaining inaccurate near the center line. Comparing the results of Simulation 3 with those of Simulation 4 indicates a possibility that subsequent simulations on the finer grid

Figure 22 Parcel SMD validation - Sim 3

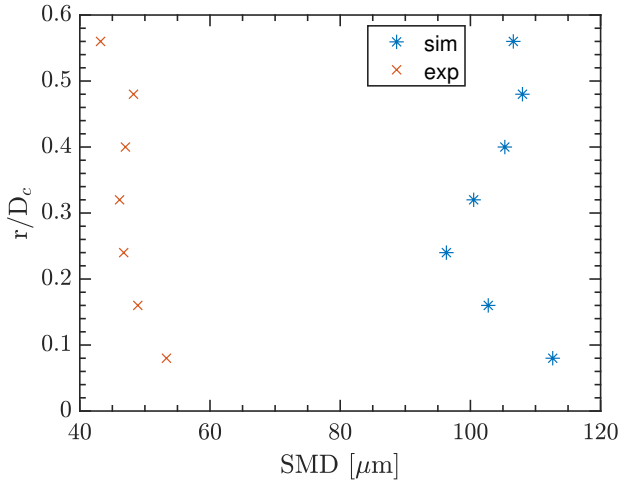

Figure 23 Parcel axial velocity validation - Sim 3

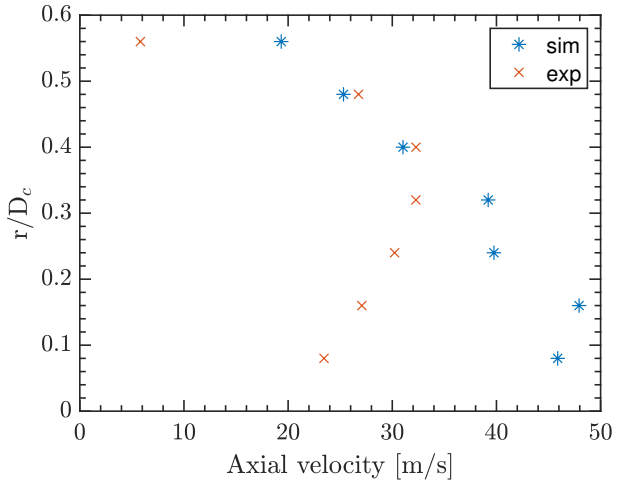

using the TAB breakup model may yield more accurate results. If the SMD values decreased by the same amount when switching to the TAB model on the fine mesh as they did on the coarse mesh, the simulation results would be roughly within 10% of experiment. In addition, the favorable shape of the axial velocity curve when using the TAB model may persist on the finer mesh and improve correlation with experiment at higher radial locations. The axial velocity values found in Fig. 23 are an improvement over those of Simulation nr. 1. Both qualitative discrepancies mentioned earlier are no longer present. Despite the improvement ,however, the velocity values near the centerline are still not in agreement with the pattern observed in the SMD values. The simulated data does not exhibit a peak at the r/D=.4 mark and there is not a decrease in velocity values from the r/D$_c$=.3 mark towards the center line. It is possible that the lack of accuracy in the diameter prediction is the primary cause for this. Empirical constants for breakup, drag and turbulent dispersion may also play a role.

There are several numerical parameters whose impact were not studied in this work. Some examples would be: asphericity criteria tolerances, turbulent dispersion time constant, breakup model constants etc. While the results presented herein are far from a complete overview of the potential of the numerical model, some conclusions can be drawn based on the presented sensitivity analyses.

5 Conclusions & Recommendations

A numerical investigation of spray formation was carried out using a recently released hybrid multi-phase solver. The solver makes use of two well-known multi-phase models (VOF and Eulerian-Lagrangian) in an attempt to capture both primary and secondary atomization in the same simulation. The solver's distinguishing feature is the set of asphericity criteria that govern the transition between multi-phase descriptions. There was a good qualitative match between the shapes of the simulated and experimentally measured SMD curves used for validation. Discrepancies were observed between simulated and measured discrete phase axial velocity curves. Significant qualitative and quantitative improvement was demonstrated with mesh refinement, however a mesh independent solution has not been achieved. The value of the presented results is therefore limited to a set of qualitative indicators/guidelines on the behaviour and accuracy potential of the studied solver. The principal findings of this study are summarized below:

- The solver can produce droplet distributions that correctly predict experimental trends
- Droplet size accuracy is directly limited by mesh resolution and permitted grid refinement levels
- The stability of the simulation is strongly affected by the OVF parameter
- The results do not show the expected trends with respect to OVF parameter variation

The subsequent paragraphs will expand on each of the findings listed above. Results suggest that the method of using geometrical criteria to identify ligaments that can be assumed to behave as a Lagrangian particle is promising. The obtained Sauter Mean Diameter distributions qualitatively match with experiment. Specifically, regions of decreases and increases in droplet diameters were correctly identified. Mesh resolution has been shown to play a key role in the accuracy of SMD and droplet velocity predictions. This plays an important role not only due to discretization error and spatial filtering, but also the multi-phase transition criteria. The grid size directly determines the smallest ligament whose shape can be resolved. A full mesh dependence study should therefore be a priority in follow-up research on the presented topic.

Regarding the OVF parameter, its role in the stability of the simulations has been noted. Its other effects could not be unambiguously identified. The results do not indicate that smaller OVF values produce smaller parcels. This is in contrast with the authors' interpretation of the role of the OVF setting. In addition, it is unclear what effects the OVF setting has on the continuum phase solution. This is primarily due to scarce documentation, but also due to conflicting simulation results (e.g. velocity/SMD correlation).

A better approach to addressing the difficulties that result from removing liquid ligaments from the Eulerian phase may be the one of Zuzio et al. (2018). A hybrid solver is described with a similar working mechanism as the one addressed in this work: transition from Eulerian to Lagrangian descriptions based on size and geometrical criteria. The key difference is in the transition process. Droplets that span several cells are not immediately approximated as a volumeless Lagrangian particle. Instead, a spherical particle is defined with a given radius, based on how many cells the liquid ligament occupies and a center of mass. Cells that are within the given radius retain liquid properties in the momentum equation. The velocity of the droplet is interpolated using velocities of surrounding cells. At this point, the interface is no longer tracked. When the droplet travels to a coarse enough region where the liquid inclusion radius is smaller than the grid size, the volumeless Lagrangian description is employed. This method may avoid the instabilities associated with the OVF parameter of the solver described herein.

The study presented in this paper makes use of a number of simplifications. Exploring their validity could be the topic of further research. One of these is the use of turbulence models derived for single-phase flows. The work of Ketterl and Klein (2018) explains the importance of interaction between turbulence and the gas/liquid interface in multi-phase flows. Specifically, it is argued that the accuracy of multiphase LES depends on the mentioned interaction. The inadequacy of classical SGS models such as the WALE model used for this study stems from the assumption that subgrid fluctuations are formed via direct energy cascade. However, liquid structures are not necessarily formed on large scales. Subgrid fluctuations caused by interaction with the interface are not accounted for (Ketterl and Klein, 2019). The authors further state that research on multi-phase LES is still in its infancy and evaluate several SGS models derived for multi-phase flows. In subsequent studies the governing equations for different SGS models are presented and analyzed (Ketterl, 2019; Klein, 2019). Results using different multi-phase SGS models are compared with data obtained via DNS for the breakup of a round liquid jet. It is concluded that the convective SGS closure strongly affects numerical stability. Two models are identified as numerically stable candidates with promising results (Ketterl, 2019). These are: a modification of Clarks model (Clark, 1979) and the sigma model (Nicoud, 2011). It is possible that the

implementation of such SGS models in hybrid multi-phase solvers, such as the one discussed herein, may yield more accurate velocity and droplet distribution results.

Despite its shortcomings, the working principle of the solver is sound. Results indicate the potential of such a hybrid multi-phase solver to produce accurate droplet distribution data using only upstream conditions as an input. The computational cost of the method is also reasonable given the cell counts and hardware used during the study. It can be anticipated that similar hybrid methods are the future for numerical simulation of spray formation.

References

Anez, J., Ahmed, A., Hecht, N., Duret, B., Reveillon, J., and Demoulin, F. (2019) 'Eulerian-–Lagrangian spray atomization model coupled with interface capturing method for diesel injectors', *International Journal of Multiphase Flow*, Vol. 113, pp.325-–342.

Baltussen, M.W., Kuipers J.A.M. and Deen, N.G. (2018) 'A critical comparison of surface tension models for the volume of fluid method', *Chemical Engineering Science*, Vol. 109, pp.65—74.

The University of Sydney, Clean Combustion Research Group. [online] http://web.aeromech.usyd.edu.au/thermofluids /database.php (Accessed 6 August 2019)

Clark, R.A., Ferziger, J.H., Reynolds, W.C. (1979) 'Evaluation of subgrid-scale models using an accurately simulated turbulent flow', *Journal of Fluid Mechanics*, Vol. 91, No. 1, pp.1-16.

Dannenhoffer, I.J., Baron, J. (1985) 'Grid adaptation for the 2-D Euler equations', *23rd Aerospace Sciences Meeting*

Ansys Fluent Theory Guide version 19.2. [online] https://ansyshelp.ansys.com/ (Accessed 20 July 2019).

Gaillard, P., Le Touze, C., Matuszewski, L., Murrone., A. (2016) 'Numerical Simulation of Cryogenic Injection in Rocket Engine Combustion Chambers', *AerospaceLab*, No. 11, pp.218–228.

Gosman, A.D., Loannides, E. (1983) 'Aspects of Computer Simulation of Liquid-Fueled Combustors', *Journal of Energy*, Vol. 7, pp.482-–490.

Herrmann, M. (2010) 'A parallel Eulerian interface tracking/Lagrangian point particle multi-scale coupling procedure', *Journal of Computational Physics*, Vol. 229, No. 3, pp.745-–759.

Hirt, C., Nichols, B. (1981) 'Volume of fluid (VOF) method for the dynamics of free boundaries', *Journal of Computational Physics*, Vol. 39, pp.201-–225.

Ketterl, S. and Klein, M. (2018) ' A-priori assessment of subgrid scale models for large-eddy simulation of multiphase primary breakup', *Computers and Fluids*, Vol. 165, pp.64-–77.

Ketterl, S., Reißmann, M., Klein, M. (2019) 'Large eddy simulation of multiphase flows using the volume of fluid method: Part 2 — A-posteriori analysis of liquid jet atomization', *Experimental and Computational Multiphase Flow*, Vol. 1, No. 3, pp.201-–211.

Klein, M., Ketterl, S., Hasslberger, J. (2019) 'Large eddy simulation of multiphase flows using the volume of fluid method: Part 1 — Governing equations and a priori analysis', *Experimental and Computational Multiphase Flow*, Vol. 1, No. 2, pp.130-–144.

Lefebvre, A. H. and McDonell, V. G. (2017) *Atomization and sprays*. 2^{nd} ed., CRC Press, Boca Raton

Lowe, A. (2018) Flow And Temperature-Field Structure of Turbulent Spray Flames: From Dilute to Dense. PhD thesis, The University of Sydney, Sydney, Australia.

Menter, F.R. (2018) 'Stress-blended eddy simulation (SBES)—A new paradigm in hybrid RANS-LES modeling', *Notes on Numerical Fluid Mechanics and Multidisciplinary Design*, Vol. 137, pp.27–37.

Menter, F.R. (1994) 'Two-equation eddy-viscosity turbulence models for engineering applications', *AIAA Journal*, Vol. 32, pp.1598-–1605.

Millikan, C.B., (1938) 'A critical discussion of turbulent flows in channels and circular tubes', *Proc. 5th Int. Congress of Appl. Mech.*, pp.386-–392.

Morsi, S.A. and Alexander, A.J. (1972) 'An investigation of particle trajectories in two-phase flow systems', *Journal of Fluid Mechanics*, Vol. 55, No. 2 pp.193-–208.

Nicoud, F., Ducros, F. (1999) 'Subgrid-scale stress modelling based on the square of the velocity gradient tensor', *Flow, Turbulence and Combustion*, Vol. 62 , No. 3, pp.183–200.

Nicoud, F., Toda, H. B., Cabrit, O., Bose, S., Lee, J. (2011) 'Using singular values to build a subgrid-scale model for large eddy simulations', *Physics of Fluids*, Vol. 23 , No. 8, 085106.

O'Rourke, P.J., Amsden, A.A. (1987) 'The Tab Method for Numerical Calculation of Spray Droplet Breakup', *SAE Technical Paper 872089*

Reitz, R. (1987) 'Modeling atomization processes in high-pressure vaporizing sprays', *Atomisation Spray Technology*, Vol. 3, pp.309–337.

Saeedipour, M., Pirker, S., Bozorgi, S., and Schneiderbauer, S. (2016) 'An Eulerian–Lagrangian hybrid model for the coarse-grid simulation of turbulent liquid jet breakup', *International Journal of Multiphase Flow*, Vol. 82, pp.17-–26.

Shinjo, J., (2018). 'Recent Advances in Computational Modeling of Primary Atomization of Liquid Fuel Sprays', *Energies*, Vol. 11 , No. 11, 2971

Shur, M., Spalart, P., Strelets, M., Travin, A. (1999) 'Detached-eddy simulation of an airfoil at high angle of attack', *Engineering Turbulence Modelling and Experiments*, Vol. 4 ,pp.669-–678.

7th Workshop on Measurement and Computation of Turbulent Spray Combustion (TCS7). [online] https://www.combustioninstitute.org/ci-event/7th-workshop-on-measurement-and-computation-of-turbulent-spray-combustion-tcs7/ (Accessed 25 July 2019)

Youngs, D.L. (1987) 'An Interface Tracking Method for a 3D Eulerian Hydrodynamics Code', Atomic Weapons Research Establishment, Technical report AWRE/44/92/35

Zuzio, D., Estivalèzes J. and DiPierro, B. (2018) 'An Improved Multiscale Eulerian-Lagrangian Method for Simulation of Atomization Process', *Computers and Fluids*, Vol. 176, pp.285—301.

Nomenclature

$\dot{m}$	Mass transfer rate, kg/s
$\hat{n}$	Volume fraction gradient unit vector
$\mathcal{K}$	von Kármán constant
$\mathbf{F}$	Surface tension force, N
$\mathbf{g}$	Gravitational acceleration, m/s^2
$\mathbf{n}$	Volume fraction gradient
$\mathbf{u}$	Velocity, m/s
A	Area, m^2
a_1	Drag law constant
a_2	Drag law constant
a_3	Drag law constant
B	Overlap Layer Constant
C_d	Drag coefficient
D_c	Coflow diameter, m
D_n	Needle diameter, m
D_p	Pilot diameter, m
I	Identity matrix
M	Momentum ratio
m	Mass, kg
p	Pressure, Pa
R	Coflow stream radius, m
r_{vol}	Volume weighting parameter
Re	Reynolds number
u^*	Friction Velocity, m/s
We	Weber number
y	Distance from centerline, m
$\boldsymbol{\mathcal{T}}$	Stress tensor, Pa

Greek symbols

α	Volume fraction
μ	Dynamic viscosity, Pa s
ν	Kinematic viscosity, m$^2/s$
ρ	Density, kg/m^3
σ	Surface tension coefficient, N/m
τ	Particle relaxation time, s

Subscripts

g	Gas
l	Liquid
p	Particle
r	Relative